

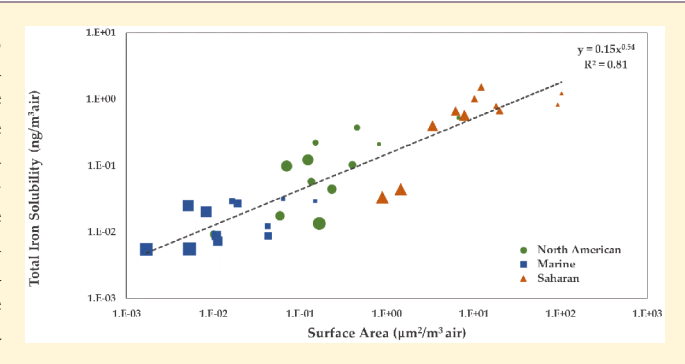
Relationship between Atmospheric Aerosol Mineral Surface Area and Iron Solubility

Mary Francis M. McDaniel,[†] Ellery D. Ingall,**,[†]

Peter L. Morton,[‡] Erin Castorina,[†] Rodney J. Weber,[†] Rachel U. Shelley, William M. Landing, Amelia F. Longo, Yan Feng, and Barry Lai

Supporting Information

ABSTRACT: Size-fractionated dust aerosols (>7.2, 7.2-3, 3-1.5, 1.5-0.95, 0.95-0.49, and $<0.49 \mu m$) originating from source regions, including the Sahara, North America, and the local marine environment, were collected shipboard in the Atlantic Ocean. Iron mineralogy, oxidation state, and solubility were examined using wet chemistry and synchrotron-based iron K-edge X-ray absorption near edge structure (XANES) spectroscopy. The soluble iron concentration showed a strong positive correlation with calculated aerosol surface area ($R^2 = 0.81$). The iron XANES spectra, for all size ranges, were nearly identical for Saharan samples. Spectra from North American and local atmosphere (marine)



provenances exhibited more variation between size fractions, with no obvious trends with the particle size. Saharan spectra were distinct from North American spectra, which confirms the different compositions of the two sources. Marine spectra displayed a range of both North American and Saharan spectral characteristics, likely reflecting that the marine samples are ultimately derived from these and potentially other sources. However, despite the notable variation in compositions, the surface area is the predominant factor affecting total iron solubility. Aerosol iron solubilization through acidic surface reactions would be most effective in samples with the highest surface area, which likely results in the strong positive correlation with soluble iron concentration in distilled water.

KEYWORDS: GEOTRACES, aerosol iron, iron solubility, surface area, synchrotron

INTRODUCTION

In many ocean regions, atmospheric aerosol deposition supplies the majority of the key micronutrient, iron. 1-8 In approximately 30% of the world's oceans, iron supply controls the growth of photosynthetic microorganisms. 1-8 The factors that control the solubility of aerosol iron and, therefore, bioavailability of iron to microorganisms remain unclear. 9-12 This has hampered our understanding of the role of aerosol iron in marine primary productivity and the associated uptake and sequestration of carbon dioxide by photosynthetic microorganisms.3,13

Studies have considered composition, reactions during transport, and anthropogenic influences as factors influencing iron solubility. Composition has been speculated to influence iron solubility in aerosols; however, a direct relationship has not been determined. 14-16 The absence of a direct relationship may reflect modification of aerosol composition during transport through reactions producing acidic species, a

modification known as acid processing.¹⁷⁻²⁴ Such reactions are often coupled with photoreduction and organic ligand reactions and typically result in increased levels of soluble iron in aerosols. 24-30 These acidic reactions that increase iron solubility are prevalent in regions with high levels of anthropogenic gases, such as SO_2 . $^{17,27,31-39}$ Inclusion of anthropogenic sources of iron related to combustion processes in atmospheric models better explains observed global trends of relative iron solubility. 40 The interplay of these factors confounds direct attribution of increased aerosol iron solubility to just one process.

Regardless of aerosol composition or anthropogenic influences, acid-processing reactions that increase iron

Received: May 30, 2019 Revised: September 18, 2019 Accepted: September 18, 2019 Published: September 18, 2019

[†]School of Earth and Atmospheric Sciences, Georgia Institute of Technology, 311 Ferst Drive, Atlanta, Georgia 30332-0340, United

^{*}National High Magnetic Field Laboratory, 1800 East Paul Dirac Drive, Tallahassee, Florida 32310, United States;

[§]Earth, Ocean and Atmospheric Science, Florida State University, Tallahassee, Florida 32306-4520, United States;

[∥]Environmental Science Division and [⊥]Advanced Photon Source, Argonne National Laboratory, 9700 South Cass Avenue, Argonne, Illinois 60439, United States;

solubility are dependent upon the surface area available for potential reaction. Previous studies have investigated parameters related in part to surface area, such as particle size 16,41,42 and surface area/volume ratio. Buck et al. found that the absolute aerosol particle size, in general, did not correlate to the soluble iron concentration. In contrast, Ooki et al. found that fractional iron solubility (ratio of soluble iron concentration/total iron concentration of the sample) increased with decreasing size, inferring that smaller size fractions were enriched with Fe(II) species. Although the enrichment of Fe(II) in smaller particles was not directly measured, the studies of Johansen and Hoffman and Johansen et al. discovered that 86% of Fe(II) present in the aerosols occurred in particles with a diameter less than 3 μ m.

In urban aerosols as a result of a combination of factors, peak metal solubility was associated with 2.5 μ m sized particles rather than the smaller or larger particles. ⁴² Baker and Jickells ⁴³ highlighted the surface area/volume ratio of aerosol particles as a primary control on aerosol iron fractional solubility. On the basis of these earlier studies, the influence of aerosol surface area on iron solubility is unclear. This study directly evaluates the relationship between the aerosol surface area and soluble iron concentration.

METHODS

Sampling. Samples were collected shipboard in the Atlantic Ocean during the 2011 U.S. GEOTRACES GA03 Atlantic transect using trace metal clean protocols. 45 Along the transect, dependent upon the prevailing wind direction, particle collectors received aerosols from three primary sources: North America, the Sahara, or slack air coming from an undefined location, which is referred to here as the marine environment. The origin of aerosols collected during each sampling event was constrained using Hybrid Single Particle Lagrangian Integrated Trajectory (HYSPLIT) model back trajectories using the Global Data Assimilation System (GDAS) half-degree meteorological archive. 46,47 HYSPLIT back trajectories were calculated at 0, 500, and 1000 m above ground level to confirm North American, Saharan, and/or marine provenances. Two sampling locations from each of these three source regions were chosen as representative samples, for a total of six sampling locations (Table 1).

Table 1. Latitude, Longitude, and Collection Dates of the Selected Sampling Locations Targeted in This Study

	sample ID	latitude (N)	longitude (W)	collection dates
North American	6319	39.35	69.54	11.08-09.2011
	6677	37.58	68.40	11.13-15.2011
marine	7156	29.70	56.82	11.21-24.2011
	7245	27.58	49.63	11.24-26.2011
Saharan	7860	22.38	35.87	12.04-05.2011
	7946	20.88	32.62	12.06-07.2011

Size-fractionated aerosols were collected simultaneously using a volumetric-flow-controlled (VFC) high-volume sampler (TE-5170VBL, Tisch Environmental)⁴⁸ mounted on the deck above the bridge on the R/V Knorr. To avoid contamination from the exhaust of the ship, the samplers paused collecting when the wind speed was less than 0.5 m s⁻¹ and when the wind direction was outside $\pm 60^{\circ}$ from the bow. The VFC sampler collected aerosols by filtering air at a flow

rate of ca. 1.2 m³ min⁻¹ over 24-72 h integration periods, yielding approximately 1400 m³ of filtered air. Size-fractionated aerosols were collected using a Sierra-type (high-volume) slotted cascade five-stage impactor (TE-235, Tisch Environmental). This impactor was loaded with Whatman 41 (W41) filters, to yield a sample set with five nominal particle aerodynamic diameter cut-offs of >7.2, >3, >1.5, >0.95, and >0.49 μ m, with an additional 20 \times 25 cm W41 sheet as a backing filter to collect ultrafine ($<0.49 \mu m$) aerosols. Sample flow passing through the impactors in the cutoff sequence listed above, followed by a final filter, results in filters with particles collected in aerodynamic diameter ranges of >7.2, 7.2-3, 3-1.5, 1.5-0.95, and 0.95-0.49 μ m and all particles smaller than 0.49 μ m. Blanks were collected from Whatman filters loaded into the sampler for 1 h when it was not in operation. Immediately after each sampling event, all aerosol samples were transported in clean plastic bins to a highefficiency particulate air (HEPA)-filtered clean lab space, where they were transferred to new zipper-type plastic bags, kept in the dark, and frozen at -20 °C until analysis.

W41 mixed cellulose ester filters were used as a result of their low trace element background levels. 48–50 The efficiency of particle collection has been shown to be high for W41 filters, up to 99% for larger particles, and up to 95% for 0.2 μ m particles. Filters were acid-washed prior to sampling using the methods outlined by Morton et al. This method consisted of acid-washing filters in 0.5 M quartz-distilled HCl (q-HCl) for 24 h at room temperature. After the acid bath, the filters were soaked in 2 L of ultrahigh-purity (UHP) water for 24 h and then transferred to a fresh acid bath. This process was repeated 3 times. Subsequently, the filters were soaked in fresh UHP water baths for 24 h 5–6 times until the pH matched that of fresh UHP water (pH 5.4–5.6). Finally, the filters were rinsed with flowing UHP water, dried for 12 h, and stored in new plastic zipper bags.

Elemental Analysis. Aerosol samples were processed for water-soluble and total elemental concentrations as detailed by Shelley et al.⁴⁵ and Morton et al.⁴⁸ Briefly, size-fractionated aerosols from each impactor stage were subdivided into nine equivalent component strips. 48 Water-soluble elements were leached from the filter strips by loading the filter sample into a 47 mm polysulfone vacuum filtration rig (Thermo Scientific Nalgene p/n 300-4100) with an acid-washed (1.2 M HCl) 0.02 μ m GN6 backing filter. While under vacuum (~6 psi), 100 mL of fresh UHP water was poured slowly over the filter. In this way, the instantaneously soluble fraction was leached from the aerosol material into a reservoir below the filter. The 100 mL of leachate was carefully decanted into an acid-washed low-density polyethylene bottle and acidified to 0.024 M HCl for storage and analysis. Replicate analyses of size-fractionated impactor strips from this study were determined to produce relative standard deviations of ~38% for soluble Fe. Uncertainty in aerosol iron solubility measurements using a variety of extraction protocols has been considered in detail⁵³ and is within the range of the error of other solubility experiments.

Total elemental concentrations were determined on size-fractionated samples by digesting filter subsamples using a digestion procedure as detailed by Shelley et al. 45 and Morton et al. 48 Briefly, filter subsamples were digested using a combination of hot HNO₃, H_2O_2 , and HF. Final digest solutions were taken to dryness and redissolved in 0.32 M HNO₃ (\sim 2%) for analysis. Both water-soluble and total

Table 2. Elemental Concentrations and Calculated Surface Area for Samples from Each Site Based on the Diameters of the Aerosols Captured on the Filters

aerosol size (µm)	Al $(ng/m^3 \text{ of air})$	total Fe (ng/m³ of air)	soluble Fe (ng/m³ of air)	surface area $(m^2/m^3 \text{ of a}$
		6319 North Amer	ica	
>7.2	44.6 ± 14.3	24.9 ± 9.2	0.013 ± 0.005	1.67×10^{-7}
7.2-3.0	21.5 ± 6.9	17.2 ± 6.4	0.122 ± 0.046	1.25×10^{-7}
3.0-1.5	18.2 ± 5.8	13.4 ± 5.0	0.045 ± 0.017	2.31×10^{-7}
1.5-0.95	17.5 ± 5.6	13.9 ± 5.1	0.103 ± 0.039	3.96×10^{-7}
0.95-0.49	11.4 ± 3.7	10.0 ± 3.7	0.374 ± 0.142	4.53×10^{-7}
< 0.49	39.0 ± 12.5	25.4 ± 9.4	0.524 ± 0.199	6.72×10^{-6}
		6677 North Amer	ica	
>7.2	2.69 ± 0.86	1.81 ± 0.67	0.009 ± 0.004	1.01×10^{-8}
7.2-3.0	12.2 ± 3.9	8.12 ± 3.00	0.097 ± 0.037	7.06×10^{-8}
3.0-1.5	4.59 ± 1.47	2.56 ± 0.95	0.018 ± 0.007	5.85×10^{-8}
1.5-0.95	5.94 ± 1.90	4.25 ± 1.57	0.058 ± 0.022	1.34×10^{-7}
0.95-0.49	3.79 ± 1.21	2.79 ± 1.03	0.223 ± 0.085	1.50×10^{-7}
<0.49	4.75 ± 1.52	3.30 ± 1.22	0.211 ± 0.080	8.19×10^{-7}
		7156 Marine		
>7.2	0.455 ± 0.146	0.554 ± 0.205	0.005 ± 0.002	1.71×10^{-9}
7.2-3.0	1.44 ± 0.46	1.04 ± 0.38	0.020 ± 0.008	8.34×10^{-9}
3.0-1.5	0.855 ± 0.274	0.753 ± 0.279	0.009 ± 0.003	1.09×10^{-8}
1.5-0.95	0.843 ± 0.270	0.739 ± 0.274	0.027 ± 0.010	1.91×10^{-8}
0.95-0.49	0.417 ± 0.133	0.519 ± 0.192	0.029 ± 0.011	1.65×10^{-8}
< 0.49	0.873 ± 0.279	0.536 ± 0.198	0.029 ± 0.011	1.51×10^{-7}
		7245 Marine		
>7.2	1.44 ± 0.46	0.574 ± 0.212	0.005 ± 0.002	5.39×10^{-9}
7.2-3.0	0.891 ± 0.29	1.01 ± 0.37	0.025 ± 0.009	5.18×10^{-9}
3.0-1.5	0.890 ± 0.28	0.653 ± 0.242	0.007 ± 0.003	1.13×10^{-8}
1.5-0.95	1.88 ± 0.60	0.878 ± 0.325	0.009 ± 0.003	4.25×10^{-8}
0.95-0.49	1.07 ± 0.34	0.592 ± 0.219	0.012 ± 0.005	4.25×10^{-8}
<0.49	0.372 ± 0.119	0.521 ± 0.193	0.031 ± 0.012	6.41×10^{-8}
		7860 Sahara		
>7.2	387 ± 124	198 ± 73	0.044 ± 0.017	1.45×10^{-6}
7.2-3.0	1350 ± 432	715 ± 264	0.567 ± 0.215	7.87×10^{-6}
3.0-1.5	955 ± 306	512 ± 190	1.508 ± 0.573	1.21×10^{-5}
1.5-0.95	875 ± 280	482 ± 179	0.669 ± 0.254	1.98×10^{-5}
0.95-0.49	463 ± 148	259 ± 96	0.781 ± 0.297	1.83×10^{-5}
<0.49	600 ± 192	325 ± 120	1.21 ± 0.46	1.03×10^{-4}
		7946 Sahara		
>7.2	237 ± 76	167 ± 62	0.033 ± 0.013	8.90×10^{-7}
7.2-3.0	585 ± 187	401 ± 148	0.395 ± 0.150	3.40×10^{-6}
3.0-1.5	490 ± 157	332 ± 123	0.663 ± 0.252	6.23×10^{-6}
1.5-0.95	450 ± 144	300 ± 111	1.01 ± 0.39	1.02×10^{-5}
< 0.49	543 ± 174	347 ± 128	0.817 ± 0.311	9.37×10^{-5}

solutions were analyzed by high-resolution inductively coupled plasma mass spectrometry (HR-ICP-MS, Element 2, Thermo), and the concentrations were quantified using matrix-matched external standards. The stage 5 impactor on sample 7946 became contaminated during analysis, and thus, the solubility results from this filter are not included in our discussion. Replicate analyses from this study were determined to produce relative standard deviations of \sim 32% for total Re

Surface Area. Using the measured total mass of aluminum on the filter and the average crustal abundance of aluminum of 8.23%, ⁵⁴ the total mass of aerosol originating from crustal material on each filter was estimated. The molar iron/aluminum ratio (calculated from Table 2 and included in Table S1 of the Supporting Information) for all size fractions and all regions fell within the expected value for continental crust (0.30 \pm 0.16), which supports the use of average crustal

abundance for aluminum. To obtain an approximate aerosol surface area, particles are assumed to be spherical, with the understanding that actual aerosol particle morphology is diverse. Aerosol particle volume was calculated using the geometric mean of the aerosol size ranges as the approximate particle radius. For the largest size fraction, the minimum size was used as the approximate particle radius. For the smallest size fraction, the geometric mean between the sampling cutoff of 0.49 μ m and a near zero value of 0.01 μ m was used as the approximate particle radius. This particle volume, an average upper continental crustal density of 2.7 g/cm³, and total aerosol mass were used to calculate the total number of aerosol particles on each filter. The total aerosol surface area was calculated using the number of particles multiplied by the average particle surface area.

Synchrotron Measurements. Iron K-edge X-ray absorption near edge structure (XANES) spectroscopy at the

ACS Earth and Space Chemistry

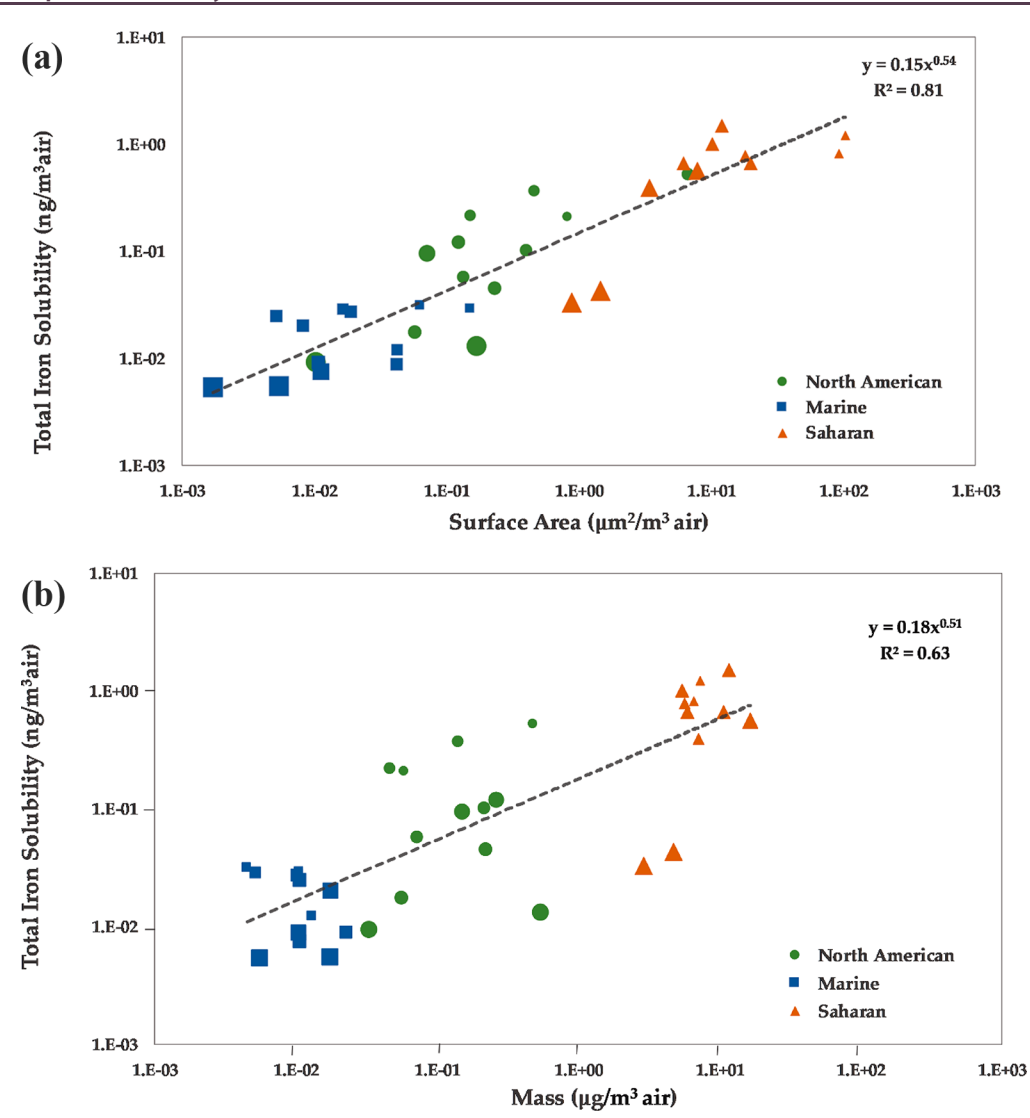


Figure 1. (a) Total soluble iron concentration versus calculated aerosol surface area. Size of the symbols represents the particle size, with larger symbols representing the larger particle sizes. (b) Total soluble iron concentration versus total aerosol mass on each filter, with larger symbol sizes representing larger particle sizes. The lower correlation of total iron solubility for mass, as opposed to surface area, is demonstrated here.

Advanced Photon Source, Station 2-ID-D at the Argonne National Laboratory, was used to identify aerosol iron characteristics. Absorption and fluorescence caused by interactions with the air were reduced by performing all measurements under a helium atmosphere. An energydispersive Si-drift detector, Vortex EM, with a 12.5 μ m Be window and a 50 mm² sensitive area, was used to measure Xray fluorescence of the samples. Spectroscopy scans were run from 7100 to 7180 eV in 0.5 eV steps with a dwell time per step of 0.3-5 s. To measure the average spectra for each sample, beamline focusing optics, including the zone plate and the order-sorting aperture, were removed for these analyses, resulting in a beam area of approximately 0.4 mm². The energy was calibrated using an iron foil standard aligned to an energy of 7112 eV at the inflection point of the absorption edge. The higher sensitivity and lower background fluorescence signal was used for aerosols in this study; hence, the term iron nearedge X-ray fluorescence spectroscopy (Fe-NEXFS) is more precise. Fe-NEXFS records a fluorescence signal, which is inversely proportional to the XANES signal. Although Fe-NEXFS was measured, this term is not as widely used;

therefore, the more common term of XANES is applied here. Spectral data were normalized to account for variations in incoming X-ray flux and were normalized to create a relative intensity value of approximately 1 for the post-edge area of the spectra for comparison to standard spectra. The data were also processed using a three-point smoothing algorithm built into the software package Athena to remove high-frequency noise. Iron mineralogy and oxidation state can be investigated using spectroscopic techniques. Pepeated scans of selected samples showed no changes in spectral characteristics, indicating that changes in the oxidation state were not occurring during analysis.

Oxidation State. The pre-edge centroid position of the bulk aerosol spectra was used to calculate the abundance of Fe(II) using the equation and procedures from Oakes et al.⁶² Previous studies have shown that using the pre-edge centroid position to indicate the oxidation state for iron is more reliable than using the position of the absorption edge.⁶²⁻⁶⁴

Linear Combination Fitting (LCF). The iron XANES spectra were characterized using the LCF algorithm in Athena. Samples with high noise relative to signal, as identified by

spectra with peak iron counts below 1700, were removed from the sample set prior to LCF. LCF to determine unknown XANES spectra was processed with a robust database of 22 known iron mineral standards that were run on the same beamline as the samples. 62,65 Initially, spectral fitting was performed using the entire database. After this initial analysis, the best fitting standards were chosen to constrain the database. After the database was narrowed, fits were performed, permitting three and then four combinatorics, depending upon the quality of the R factor (the lowest R factor indicates the best linear combination fit⁵⁸). Through this iterative process for each sample, the linear combination fits were selected, which yielded a low R factor, excluding the standards within these iterations that comprised less than 10%. The R factor, computed by Athena using a nonlinear, least squares minimization process with the standard spectra to fit the unknown samples, yields the goodness of a linear combination fit.

■ RESULTS AND DISCUSSION

The soluble iron concentration, which covers 3 orders of magnitude, exhibits a positive relationship ($R^2 = 0.81$) with the surface area of crustal material for the three source regions (Figure 1a). The relationship between the surface area and soluble iron concentration can be fit by eq 1.

$$y = 0.15x^{0.54} \tag{1}$$

A relation between estimated aerosol mass and soluble iron concentration might also be expected, because samples with higher iron contents would have more iron available for solubilization. However, the soluble iron concentration plotted as a function of the calculated aerosol mass has a lower correlation ($R^2 = 0.63$) than the relation with surface area (Figure 1b). This is consistent with the idea that reactions solubilizing iron in aerosols are focused on particle surfaces that are most accessible to acid processing, 20 photoreduction, 2 and ligand-promoted iron solubilization processes. 12 Similarly, surface area/volume ratios could be an indication of iron solubility, 66 but the surface area/volume ratio leads to a R² correlation of only 0.63 (Figure S2 of the Supporting Information). Although both aerosol mass and surface area/ volume ratios can indicate a relationship to iron solubility, we demonstrate here that surface area is a simpler and possibly more accurate indicator of total iron solubility.

The trend in Figure 1a may be influenced by compositional differences. A comparison of the features of iron XANES spectra can be used to assess compositional similarities or differences between samples. To ascribe specific mineral information to spectra, LCF with known iron-containing standards is often employed. 67,68 Unfortunately, the somewhat featureless nature of the bulk aerosol spectra of this study precludes reliable identification of specific mineral phases with linear combination fits. 67-69 LCF of aerosol XANES spectra revealed that aerosol composition in all sizes is a mix of compounds, as shown in the Table S2 of the Supporting Information. The sources were best matched by a mix of iron phosphates, iron sulfates, and iron oxides, with occasional occurrences of iron silicates and iron-containing organics. Other than the iron oxides and silicates, major phases observed in the aerosols are not common in the source regions. For example, applying a linear fit routine to the Saharan spectra yielded results indicating the dominant presence of iron

phosphate and iron sulfate phases. Calculations based on the stoichiometry of these phases require concentrations of phosphorus or sulfur that were well above those expected from average crustal concentrations. To confirm the stoichiometry, surface analysis was performed on a few of the aerosol samples, using Thermo K-Alpha X-ray photon spectoscopy (XPS), which is described in the Supporting Information. Using XPS on a few representative samples, it was confirmed that phosphorus was not present on the surface of these samples. Raw data of the iron scans from XPS are shown in Figure S1 of the Supporting Information. Hence, the mineralogy determined from the LCF algorithm may not accurately reflect true sample composition, a finding that has been noted before⁶⁹ as a result of the similarities of spectra between different minerals (Figure S3 of the Supporting Information). Because of this, spectral characteristics alone were used to compare compositional similarity between samples rather than linear combination fits.⁷⁰

Spectra for the Saharan samples had nearly identical absorption edge positions at 7126 eV and a small peak at an energy of 7148 eV (Figure 2). The similar absorption edge

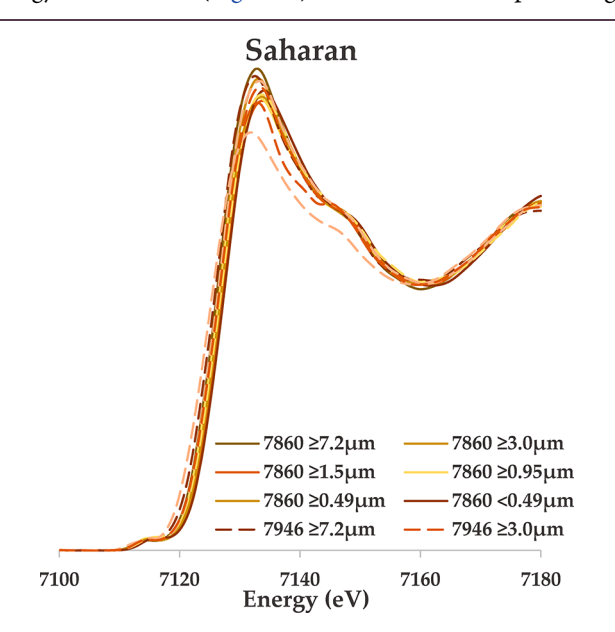


Figure 2. Saharan spectra for each size fraction sampled.

position alongside the similar location of the secondary peak implies that there is only slight variation in composition between Saharan size fractions.

North American samples had wider variation in absorption edge position ranging from 7123 to 7126 eV. Some North American spectra had a post-edge peak at 7148 eV (Figure 3). Most North American aerosol size fractions have an absorption edge position of approximately 7124 \pm 1 eV, suggesting compositional similarity among size fractions.

A comparison of absorption edge position and spectral characteristics indicates that North American and Saharan aerosols are compositionally distinct. Marine samples were defined using HYSPLIT models as having no or minimal interaction with major continental land masses within the 5 day simulation period (slack winds). Absorption edge position of the marine spectra ranged from 7123 to 7127 eV (Figure 4), which covers the range observed in the Saharan and North American spectra.

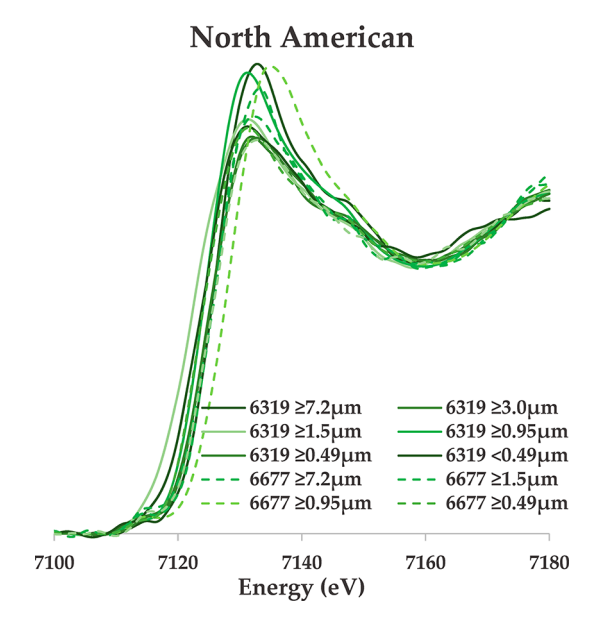


Figure 3. North American spectra for each size fraction sampled.

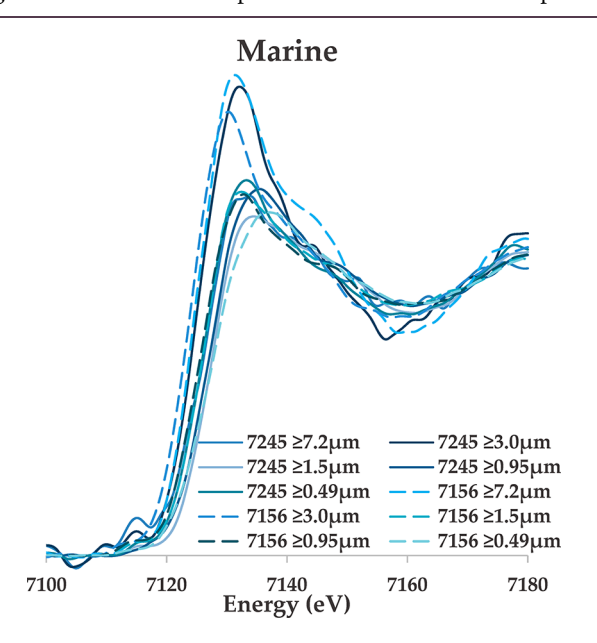


Figure 4. Marine spectra for each size fraction sampled.

On the basis of spectra, marine samples are presumed to contain a mixture of Saharan, North American, and possibly European sourced aerosols that remain in the atmosphere after a long period of slack winds. Higher energy features in the marine samples were harder to characterize. Marine samples had lower overall sample mass and, therefore, lower overall count rates, which decreased signal-to-noise ratios. In all size fractions from all sources, the iron oxidation state was predominantly Fe(III). The exception involved four marine size fractions, which contained between approximately 15 and 20% Fe(II), but the lower signal-to-noise ratios of these samples could impact the accuracy of this result. Reduced iron in marine samples has been attributed to photoreduction processes.²⁴

Different iron-containing minerals, including silicates, oxides, and sulfides, have a wide range of solubilities with respect to acid and other extractants.^{71,72} Thus, it would be expected that compositional differences as indicated by

XANES spectra would lead to strong compositional controls on solubility. However, this was not observed. One possible explanation for this discrepancy is that the spectra are measuring the form of iron distributed throughout the sample, whereas the solubility reactions will be focused on the mineral phases on the surfaces of aerosol particles. During weathering reactions in surface sediments and aerosols, iron oxides and iron sulfates form coatings on the surfaces of iron-containing minerals. 39,73,74 These surface coatings would likely comprise a small percentage of the iron mass in our aerosol samples and would thus not be a prominent result in spectral LCF. Aerosol soluble iron concentrations may reflect reaction with these coatings rather than a full range of iron-containing minerals. Presumably, such coatings have a much more limited range of solubility when compared to all iron minerals. Aerosol iron solubilization through reaction with surface coatings would be most effective in samples with the highest surface area. These data show that the aerosol surface area is a key variable in explaining the 3 orders of magnitude range of total soluble iron concentrations observed in atmospheric aerosols.

ASSOCIATED CONTENT

S Supporting Information

The Supporting Information is available free of charge on the ACS Publications website at DOI: 10.1021/acsearthspace-chem.9b00152.

Molar Fe/Al ratios (Table S1), LCF results of samples (Table S2), XPS methods, raw data from XPS scans of iron (Figure S1), total soluble Fe concentration versus the ratio of aerosol surface area/volume (Figure S2), and comparison of a typical aerosol spectrum to four reference spectra (Figure S3) (PDF)

AUTHOR INFORMATION

Corresponding Author

*Telephone: +1-404-894-3883. E-mail: ellery.ingall@eas.gatech.edu.

ORCID ®

Ellery D. Ingall: 0000-0003-1954-0317

Notes

The authors declare no competing financial interest.

ACKNOWLEDGMENTS

The authors sincerely appreciate the detailed comments of the reviewers. Many of the comments were structured in a way to enable us to substantially improve this manuscript, and we are very grateful for the investment of time and knowledge of the reviewers. This material is based on work supported by the National Science Foundation under Grants OCE-1357375 (to Ellery D. Ingall), OCE-1658181 (to Ellery D. Ingall), OCE-0929919 (to William M. Landing), OCE-1034764 (to William M. Landing), and OCE-1658311 (to Peter L. Morton). The National High Magnetic Field Laboratory is supported by the National Science Foundation through NSF/DMR-1157490 and DMR-1644779 and the State of Florida. Any opinions, findings, and conclusions or recommendations expressed in this material are those of the authors and do not necessarily reflect the views of the National Science Foundation. Use of the Advanced Photon Source and support to Yan Feng and Barry Lai are provided by the Argonne National Laboratory under the U.S. Department of Energy Contract DE-AC0206CH11357. Mary Francis M. McDaniel thanks Rutt Bridges for providing undergraduate research support through the Rutt Bridges Undergraduate Research Initiative.

REFERENCES

- (1) Martin, J. H. Glacial-Interglacial CO₂ Change: The Iron Hypothesis. *Paleoceanography* **1990**, 5 (1), 1–13.
- (2) Boyd, P. W.; Mackie, D. S.; Hunter, K. A. Aerosol iron deposition to the surface ocean—Modes of iron supply and biological responses. *Mar. Chem.* **2010**, *120* (1–4), *128*–143.
- (3) Schulz, M.; Prospero, J. M.; Baker, A. R.; Dentener, F.; Ickes, L.; Liss, P. S.; Mahowald, N. M.; Nickovic, S.; García-Pando, C. P.; Rodríguez, S.; Sarin, M.; Tegen, I.; Duce, R. A. Atmospheric Transport and Deposition of Mineral Dust to the Ocean: Implications for Research Needs. *Environ. Sci. Technol.* **2012**, *46* (19), 10390–10404
- (4) Coale, K. H.; Johnson, K. S.; Fitzwater, S. E.; Gordon, R. M.; Tanner, S.; Chavez, F. P.; Ferioli, L.; Sakamoto, C.; Rogers, P.; Millero, F.; Steinberg, P.; Nightingale, P.; Cooper, D.; Cochlan, W. P.; Landry, M. R.; Constantinou, J.; Rollwagen, G.; Trasvina, A.; Kudela, R. A massive phytoplankton bloom induced by an ecosystem-scale iron fertilization experiment in the equitorial Pacific Ocean. *Nature* 1996, 383 (6600), 495–501.
- (5) Boyd, P. W.; Watson, A. J.; Law, C. S.; Abraham, E. R.; Trull, T.; Murdoch, R.; Bakker, D. C. E.; Bowie, A. R.; Buesseler, K. O.; Chang, H.; Charette, M.; Croot, P.; Downing, K.; Frew, R.; Gall, M.; Hadfield, M.; Hall, J.; Harvey, M.; Jameson, G.; LaRoche, J.; Liddicoat, M.; Ling, R.; Maldonado, M. T.; McKay, R. M.; Nodder, S.; Pickmere, S.; Pridmore, R.; Rintoul, S.; Safi, K.; Sutton, P.; Strzepek, R.; Tanneberger, K.; Turner, S.; Waite, A.; Zeldis, J. A mesoscale phytoplankton bloom in the polar Southern Ocean stimulated by iron fertilization. *Nature* **2000**, *407* (6805), 695–702.
- (6) Buesseler, K. O.; Andrews, J. E.; Pike, S. M.; Charette, M. A. The effects of iron fertilization on carbon sequestration in the Southern Ocean. *Science* **2004**, *304* (5669), 414–417.
- (7) Coale, K. H.; Johnson, K. S.; Chavez, F. P.; Buesseler, K. O.; Barber, R. T.; Brzezinski, M. A.; Cochlan, W. P.; Millero, F. J.; Falkowski, P. G.; Bauer, J. E.; Wanninkhof, R. H.; Kudela, R. M.; Altabet, M. A.; Hales, B. E.; Takahashi, T.; Landry, M. R.; Bidigare, R. R.; Wang, X. J.; Chase, Z.; Strutton, P. G.; Friederich, G. E.; Gorbunov, M. Y.; Lance, V. P.; Hilting, A. K.; Hiscock, M. R.; Demarest, M.; Hiscock, W. T.; Sullivan, K. F.; Tanner, S. J.; Gordon, R. M.; Hunter, C. N.; Elrod, V. A.; Fitzwater, S. E.; Jones, J. L.; Tozzi, S.; Koblizek, M.; Roberts, A. E.; Herndon, J.; Brewster, J.; Ladizinsky, N.; Smith, G.; Cooper, D.; Timothy, D.; Brown, S. L.; Selph, K. E.; Sheridan, C. C.; Twining, B. S.; Johnson, Z. I. Southern ocean iron enrichment experiment: Carbon cycling in high- and low-Si waters. *Science* 2004, 304 (5669), 408–414.
- (8) de Jong, J.; Schoemann, V.; Lannuzel, D.; Croot, P.; de Baar, H.; Tison, J.-L. Natural iron fertilization of the Atlantic sector of the Southern Ocean by continental shelf sources of the Antarctic Peninsula. *J. Geophys. Res.: Biogeosci.* **2012**, *117*, G01029.
- (9) Jickells, T. D.; An, Z. S.; Andersen, K. K.; Baker, A. R.; Bergametti, G.; Brooks, N.; Cao, J. J.; Boyd, P. W.; Duce, R. A.; Hunter, K. A.; Kawahata, H.; Kubilay, N.; la Roche, J.; Liss, P. S.; Mahowald, N.; Prospero, J. M.; Ridgwell, A. J.; Tegen, I.; Torres, R. Global iron connections between desert dust, ocean biogeochemistry, and climate. *Science* **2005**, 308 (5718), 67–71.
- (10) Mahowald, N. M.; Baker, A. R.; Bergametti, G.; Brooks, N.; Duce, R. A.; Jickells, T. D.; Kubilay, N.; Prospero, J. M.; Tegen, I. Atmospheric global dust cycle and iron inputs to the ocean. *Global Biogeochemical Cycles* **2005**, *19* (4), GB4025.
- (11) Meskhidze, N.; Johnson, M. S.; Hurley, D.; Dawson, K. Influence of measurement uncertainties on fractional solubility of iron in mineral aerosols over the oceans. *Aeolian Res.* **2016**, *22*, 85–92.
- (12) Baker, A. R.; Croot, P. L. Atmospheric and marine controls on aerosol iron solubility in seawater. *Mar. Chem.* **2010**, *120*, 4–13.

- (13) Spolaor, A.; Vallelonga, P.; Cozzi, G.; Gabrieli, J.; Varin, C.; Kehrwald, N.; Zennaro, P.; Boutron, C.; Barbante, C. Iron speciation in aerosol dust influences iron bioavailability over glacial-interglacial timescales. *Geophys. Res. Lett.* **2013**, *40*, 1618–1623.
- (14) Journet, E.; Desboeufs, K. V.; Caquineau, S.; Colin, J. L. Mineralogy as a critical factor of dust iron solubility. *Geophys. Res. Lett.* **2008**, 35 (7), 5–L07805.
- (15) Fu, H. B.; Shang, G. F.; Lin, J.; Hu, Y. J.; Hu, Q. Q.; Guo, L.; Zhang, Y. C.; Chen, J. M. Fractional iron solubility of aerosol particles enhanced by biomass burning and ship emission in Shanghai, East China. *Sci. Total Environ.* **2014**, *481*, 377–391.
- (16) Buck, C. S.; Landing, W. M.; Resing, J. A. Particle size and aerosol iron solubility: A high-resolution analysis of Atlantic aerosols. *Mar. Chem.* **2010**, *120* (1–4), 14–24.
- (17) Solmon, F.; Chuang, P. Y.; Meskhidze, N.; Chen, Y. Acidic processing of mineral dust iron by anthropogenic compounds over the north Pacific Ocean. *J. Geophys. Res.: Atmos.* **2009**, *114*, D02305.
- (18) Zhuang, G.; Yi, Z.; Duce, R. A.; Brown, P. R. Link between iron and sulphur cycles suggested by detection of Fe(II) in remote marine aerosols. *Nature* **1992**, 335 (6360), 537–539.
- (19) Longo, A. F.; Feng, Y.; Lai, B.; Landing, W. M.; Shelley, R. U.; Nenes, A.; Mihalopoulos, N.; Violaki, K.; Ingall, E. D. Influence of Atmospheric Processes on the Solubility and Composition of Iron in Saharan Dust. *Environ. Sci. Technol.* **2016**, *50* (13), 6912–6920.
- (20) Shi, Z.; Krom, M. D.; Jickells, T. D.; Bonneville, S.; Carslaw, K. S.; Mihalopoulos, N.; Baker, A. R.; Benning, L. G. Impacts on iron solubility in the mineral dust by processes in the source region and the atmosphere: A review. *Aeolian Res.* **2012**, *5*, 21–42.
- (21) Ito, A.; Feng, Y. Role of dust alkalinity in acid mobilization of iron. *Atmos. Chem. Phys.* **2010**, *10* (19), 9237–9250.
- (22) Johansen, A. M.; Siefert, R. L.; Hoffmann, M. R. Chemical composition of aerosols collected over the tropical North Atlantic Ocean. *Journal of Geophysical Research-Atmospheres* **2000**, *105* (D12), 15277–15312.
- (23) Ravelo-Perez, L. M.; Rodriguez, S.; Galindo, L.; Garcia, M. I.; Alastuey, A.; Lopez-Solano, J. Soluble iron dust export in the high altitude Saharan Air Layer. *Atmos. Environ.* **2016**, *133*, 49–59.
- (24) Ingall, E.; Feng, Y.; Longo, A.; Lai, B.; Shelley, R.; Landing, W.; Morton, P.; Nenes, A.; Mihalopoulos, N.; Violaki, K.; Gao, Y.; Sahai, S.; Castorina, E. Enhanced Iron Solubility at Low pH in Global Aerosols. *Atmosphere* **2018**, *9* (5), 201.
- (25) Zhu, X.; Prospero, J. M.; Savoie, D. L.; Millero, F. J.; Zika, R. G.; Saltzman, E. S. Photoreduction of iron(III) in marine mineral aerosol solutions. *Journal of Geophysical Research-Atmospheres* **1993**, 98 (D5), 9039–9046.
- (26) Paris, R.; Desboeufs, K. V.; Journet, E. Variability of dust iron solubility in atmospheric waters: Investigation of the role of oxalate organic complexation. *Atmos. Environ.* **2011**, *45* (36), 6510–6517.
- (27) Nenes, A.; Krom, M. D.; Mihalopoulos, N.; Van Cappellen, P.; Shi, Z.; Bougiatioti, A.; Zarmpas, P.; Herut, B. Atmospheric acidification of mineral aerosols: A source of bioavailable phosphorus for the oceans. *Atmos. Chem. Phys.* **2011**, *11* (13), 6265–6272.
- (28) Johnson, M. S.; Meskhidze, N. Atmospheric dissolved iron deposition to the global oceans: Effects of oxalate-promoted dissolution, photochemical redox cycling, and dust mineralogy. *Geosci. Model Dev.* **2013**, *6*, 1137–1155.
- (29) Wozniak, A. S.; Shelley, R. U.; Sleighter, R. L.; Abdulla, H. A. N.; Morton, P. L.; Landing, W. M.; Hatcher, P. G. Relationships among aerosol water soluble organic matter, iron and aluminum in European, North African, and Marine air masses from the 2010 US GEOTRACES cruise. *Mar. Chem.* 2013, 154, 24–33.
- (30) Wozniak, A. S.; Shelley, R. U.; McElhenie, S. D.; Landing, W. M.; Hatcher, P. G. Aerosol water soluble organic matter characteristics over the North Atlantic Ocean: Implications for iron-binding ligands and iron solubility. *Mar. Chem.* 2015, 173, 162–172.
- (31) Srinivas, B.; Sarin, M. M.; Kumar, A. Impact of anthropogenic sources on aerosol iron solubility over the Bay of Bengal and the Arabian Sea. *Biogeochemistry* **2012**, *110* (1–3), 257–268.

- (32) Sholkovitz, E. R.; Sedwick, P. N.; Church, T. M. Influence of anthropogenic combustion emissions on the deposition of soluble aerosol iron to the ocean: Empirical estimates for island sites in the North Atlantic. *Geochim. Cosmochim. Acta* **2009**, 73 (14), 3981–4003.
- (33) Takahashi, T.; Furukawa, T.; Kanai, Y.; Uematsu, M.; Zheng, G.; Marcus, M. A. Seasonal changes in Fe species and soluble Fe concentration in the atmosphere in the Northwest Pacific region based on the analysis of aerosols collected in Tsukuba, Japan. *Atmos. Chem. Phys.* **2013**, *13*, 7695–7710.
- (34) Oakes, M.; Ingall, E. D.; Lai, B.; Shafer, M. M.; Hays, M. D.; Liu, Z. G.; Russell, A. G.; Weber, R. J. Iron Solubility Related to Particle Sulfur Content in Source Emission and Ambient Fine Particles. *Environ. Sci. Technol.* **2012**, *46* (12), 6637–6644.
- (35) Meskhidze, N.; Chameides, W. L.; Nenes, A. Dust and pollution: A recipe for enhanced ocean fertilization? *J. Geophys. Res.:* Atmos. 2005, 110, D03301.
- (36) Meskhidze, N.; Chameides, W. L.; Nenes, A.; Chen, G. Iron mobilization in mineral dust: Can anthropogenic SO₂ emissions affect ocean productivity? *Geophys. Res. Lett.* **2003**, *30* (21), 1–5.
- (37) Sedwick, P.; Sholkovitz, E. R.; Church, T. M. Impact of anthropogenic combustion emissions on the fractional solubility of aerosol iron: Evidence from the Sargasso Sea. *Geochem., Geophys., Geosyst.* **2007**, *8* (10), 1–21.
- (38) Zhang, T. R.; Shi, J. H.; Gao, H. W.; Zhang, J.; Yao, X. H. Impact of source and atmospheric processing on Fe solubility in aerosols over the Yellow Sea, China. *Atmos. Environ.* **2013**, *75*, 249–256.
- (39) Li, W.; Xu, L.; Liu, X.; Zhang, J.; Lin, Y.; Yao, X.; Gao, H.; Zhang, D.; Chen, J.; Wang, W.; Harrison, R. M.; Zhang, X.; Shao, L.; Fu, P.; Nenes, A.; Shi, Z. Air pollution-aerosol interactions produce more bioavailable iron for ocean ecosystems. *Sci. Adv.* **2017**, *3* (3), e1601749.
- (40) Ito, A.; Myriokefalitakis, S.; Kanakidou, M.; Mahowald, N.; Scanza, R.; Hamilton, D.; Baker, A. R.; Jickells, T. D.; Sarin, M.; Bikkina, S.; Gao, Y.; Shelley, R. U.; Buck, C. S.; Landing, W. M.; Bowie, A. R.; Perron, M. M. G.; Guieu, C.; Meskhidze, N.; Johnson, M. S.; Feng, Y.; Kok, J. F.; Nenes, A.; Duce, R. A. Pyrogenic iron: The missing link to high iron solubility in aerosols. *Sci. Adv.* **2019**, *5* (5), eaau7671.
- (41) Ooki, A.; Nishioka, J.; Ono, T.; Noriki, S. Size dependence of iron solubility of Asian mineral dust particles. *J. Geophys. Res.: Atmos.* **2009**, *114*, D09301.
- (42) Fang, T.; Guo, H. Y.; Zeng, L. H.; Verma, V.; Nenes, A.; Weber, R. J. Highly Acidic Ambient Particles, Soluble Metals, and Oxidative Potential: A Link between Sulfate and Aerosol Toxicity. *Environ. Sci. Technol.* **2017**, *51* (5), 2611–2620.
- (43) Baker, A. R.; Jickells, T. D. Mineral particle size as a control on aerosol iron solubility. *Geophys. Res. Lett.* **2006**, *33*, L07805.
- (44) Johansen, A. M.; Hoffmann, M. R. Chemical characterization of ambient aerosol collected during the northeast monsoon season over the Arabian Sea: Labile-Fe(II) and other trace metals. *J. Geophys. Res.: Atmos.* **2003**, *108* (D14), 1–11.
- (45) Shelley, R. U.; Morton, P. L.; Landing, W. M. Elemental ratios and enrichment factors in aerosols from the US-GEOTRACES north Atlantic transects. *Deep Sea Res., Part II* **2015**, *116*, 262–272.
- (46) Stein, A. F.; Draxler, R. R.; Rolph, G. D.; Stunder, B. J. B.; Cohen, M. D.; Ngan, F. NOAA's HYSPLIT Atmospheric Transport and Dispersion Modeling System. *Bull. Am. Meteorol. Soc.* **2015**, *96* (12), 2059–2077.
- (47) Rolph, G.; Stein, A.; Stunder, B. Real-time Environmental Applications and Display sYstem: READY. *Environ. Modell. Software* **2017**, 95, 210–228.
- (48) Morton, P. L.; Landing, W. M.; Hsu, S. C.; Milne, A.; Aguilar-Islas, A. M.; Baker, A. R.; Bowie, A. R.; Buck, C. S.; Gao, Y.; Gichuki, S.; Hastings, M. G.; Hatta, M.; Johansen, A. M.; Losno, R.; Mead, C.; Patey, M. D.; Swarr, G.; Vandermark, A.; Zamora, L. M. Methods for the sampling and analysis of marine aerosols: Results from the 2008 GEOTRACES aerosol intercalibration experiment. *Limnol. Oceanogr.: Methods* 2013, 11, 62–78.

- (49) Baker, A. R.; French, M.; Linge, K. L. Trends in aerosol nutrient solubility along a west-east transect of the Saharan dust plume. *Geophys. Res. Lett.* **2006**, 33 (7), 1–4.
- (50) Baker, A. R.; Jickells, T. D.; Witt, M.; Linge, K. L. Trends in the solubility of iron, aluminium, manganese and phosphorus in aerosol collected over the Atlantic Ocean. *Mar. Chem.* **2006**, *98* (1), 43–58.
- (51) Savoie, D. L. Nitrate and non-sea-salt sulfate aerosols over major regions of the world ocean: Concentrations, sources, and fluxes. Ph.D. Thesis, University of Miami, Miami, FL, 1984.
- (52) Stafford, R. G.; Ettinger, H. J. Filter efficiency as a function of particle-size and velocity. *Atmos. Environ.* **1972**, *6* (5), 353–362.
- (53) Clough, R.; Lohan, M. C.; Ussher, S. J.; Nimmo, M.; Worsfold, P. J. Uncertainty associated with the leaching of aerosol filters for the determination of metals in aerosol particulate matter using collision/reaction cell ICP-MS detection. *Talanta* **2019**, *199*, 425–430.
- (54) Taylor, S. R. Abundance of chemical elements in the continental crust—A new table. *Geochim. Cosmochim. Acta* **1964**, 28 (AUG), 1273–1285.
- (55) Buck, C. S.; Landing, W. M.; Resing, J. A.; Measures, C. I. The solubility and deposition of aerosol Fe and other trace elements in the North Atlantic Ocean: Observations from the A16N CLIVAR/CO₂ repeat hydrography section. *Mar. Chem.* **2010**, *120* (1–4), 57–70.
- (56) Yang, P.; Feng, Q.; Hong, G.; Kattawar, G. W.; Wiscombe, W. J.; Mishchenko, M. I.; Dubovik, O.; Laszlo, I.; Sokolik, I. N. Modeling of the scattering and radiative properties of nonspherical dust-like aerosols. *J. Aerosol Sci.* **2007**, 38 (10), 995–1014.
- (57) Carmichael, R. S. Handbook of Physical Properties of Rocks, 1st ed.; CRC Press: Boca Raton, FL, 1984; Vol. 3.
- (58) Ravel, B.; Newville, M. ATHENA, ARTEMIS, HEPHAESTUS: Data analysis for X-ray absorption spectroscopy using IFEFFIT. *J. Synchrotron Radiat.* **2005**, *12*, 537–541.
- (59) Hoffmann, P.; Dedik, A. N.; Ensling, J.; Weinbruch, S.; Weber, S.; Sinner, T.; Gutlich, P.; Ortner, H. M. Speciation of iron in atmospheric aerosol samples. *J. Aerosol Sci.* **1996**, 27 (2), 325–337.
- (60) Weber, S.; Hoffmann, P.; Ensling, J.; Dedik, A. N.; Weinbruch, S.; Miehe, G.; Gutlich, P.; Ortner, H. M. Characterization of iron compounds from urban and rural aerosol sources. *J. Aerosol Sci.* **2000**, 31 (8), 987–997.
- (61) Moffet, R. C.; Furutani, H.; Rodel, T. C.; Henn, T. R.; Sprau, P. O.; Laskin, A.; Uematsu, M.; Gilles, M. K. Iron speciation and mixing in single aerosol particles from the Asian continental outflow. *J. Geophys. Res.: Atmos.* **2012**, *117*, D07204.
- (62) Oakes, M.; Weber, R. J.; Lai, B.; Russell, A.; Ingall, E. D. Characterization of iron speciation in urban and rural single particles using XANES spectroscopy and micro X-ray fluorescence measurements: Investigating the relationship between speciation and fractional iron solubility. *Atmos. Chem. Phys.* **2012**, *12* (2), 745–756.
- (63) Bajt, S.; Sutton, S. R.; Delaney, J. S. X-ray microprobe analysis of iron oxidation-states in silicates and oxides using X-ray -absorption near-edge structure (XANES). *Geochim. Cosmochim. Acta* **1994**, *58* (23), 5209–5214.
- (64) Wilke, M.; Farges, F.; Petit, P. E.; Brown, G. E.; Martin, F. Oxidation state and coordination of Fe in minerals: An FeK-XANES spectroscopic study. *Am. Mineral.* **2001**, *86* (5–6), 714–730.
- (65) Ingall, E. D.; Diaz, J. M.; Longo, A. F.; Oakes, M.; Finney, L.; Vogt, S.; Lai, B.; Yager, P. L.; Twining, B. S.; Brandes, J. A. Role of biogenic silica in the removal of iron from the Antarctic seas. *Nat. Commun.* **2013**, *4*, 1–6.
- (66) Baker, A. R.; Jickells, T. D. Mineral particle size as a control on aerosol iron solubility. *Geophys. Res. Lett.* **2006**, 33 (17), 1–4.
- (67) Hesterberg, D. Macroscale Chemical Properties and X-ray Absorption Spectroscopy of Soil Phosphorus. In *Developments in Soil Science*; Balwant, S., Markus, G., Eds.; Elsevier: Amsterdam, Netherlands, 2010; Vol. 34, Synchrotron-Based Techniques in Soils and Sediments, Chapter 11, pp 313–356, DOI: 10.1016/S0166-2481(10)34011-6.
- (68) Gräfe, M.; Donner, E.; Collins, R. N.; Lombi, E. Speciation of metal(loid)s in environmental samples by X-ray absorption spectroscopy: A critical review. *Anal. Chim. Acta* **2014**, 822, 1–22.

- (69) Da Silva-Cadoux, C.; Zanella, L.; Gaillard, J.-F. Selecting reference compounds for determining chemical speciation by X-ray absorption spectroscopy. *J. Anal. At. Spectrom.* **2012**, *27* (6), 957–965.
- (70) Piquer, C.; Laguna-Marco, M. A.; Roca, A. G.; Boada, R.; Guglieri, C.; Chaboy, J. Fe K-Edge X-ray Absorption Spectroscopy Study of Nanosized Nominal Magnetite. *J. Phys. Chem. C* **2014**, *118* (2), 1332–1346.
- (71) Canfield, D. E. Reactive iron in marine-sediments. *Geochim. Cosmochim. Acta* 1989, 53 (3), 619–632.
- (72) Raiswell, R.; Canfield, D. E. Sources of iron for pyrite formation in marine sediments. *Am. J. Sci.* **1998**, 298 (3), 219–245.
- (73) Velbel, M. A. Weathering of hornblende to ferruginous products by a dissolution-reprecipitation mechanism—Petrography and stoichiometry. *Clays Clay Miner.* **1989**, *37* (6), 515–524.
- (74) Poulton, S. W.; Raiswell, R. The low-temperature geochemical cycle of iron: From continental fluxes to marine sediment deposition. *Am. J. Sci.* **2002**, 302 (9), 774–805.